

Research



Cite this article: Ventrella FM, Pujara N, Boffetta G, Cencini M, Thiffeault J-L, De Lillo F. 2023 Microswimmer trapping in surface waves with shear. *Proc. R. Soc. A* **479**: 20230280. <https://doi.org/10.1098/rspa.2023.0280>

Received: 26 April 2023

Accepted: 13 September 2023

Subject Areas:

fluid mechanics

Keywords:

phytoplankton, microswimmers, waves, Lagrangian transport

Author for correspondence:

F. M. Ventrella

e-mail: francescomichele.ventrella@unito.it

Microswimmer trapping in surface waves with shear

F. M. Ventrella¹, N. Pujara², G. Boffetta¹,
M. Cencini^{4,5}, J.-L. Thiffeault³ and F. De Lillo¹

¹Dipartimento di Fisica and INFN, Università degli Studi di Torino, via P. Giuria 1, 10125 Torino, Italy

²Department of Civil and Environmental Engineering, and

³Department of Mathematics, University of Wisconsin–Madison, Madison, WI 53706, USA

⁴Istituto dei Sistemi Complessi, CNR, via dei Taurini 19, 00185 Rome, Italy

⁵INFN, sez. Roma2 ‘Tor Vergata’, Rome, Italy

 FMV, 0000-0001-7367-1444; NP, 0000-0002-0274-4527; GB, 0000-0002-2534-7751; MC, 0000-0001-7073-5000; J-LT, 0000-0001-7724-7966; FDL, 0000-0002-1327-695X

Many species of phytoplankton migrate vertically near the surface of the ocean, in search of either light or nutrients. These motile organisms are affected by ocean surface waves. We derive a set of wave-averaged equations to describe the motion of microswimmers with spheroidal body shapes that includes several additional effects, such as gyrotaxis, settling and wind-driven shear. In addition to the well-known Stokes drift, the microswimmer trajectories depend on their orientation in a way that can lead to trapping at a particular depth; this in turn can affect transport of organisms, and may help explain observed phytoplankton layers in the ocean.

1. Introduction

Many phytoplankton species, inhabiting lakes and oceans, are motile, an ability that allows them to migrate vertically in the water column to better exploit light, which is available near the surface, and to search for nutrients, which are typically more plentiful at depth. While migrating they must contend with the background fluid motion driven by waves, currents and turbulence. As a primary producer of biomass in aquatic ecosystems, phytoplankton supports the aquatic food web and sequesters carbon. Thus, geophysical processes

that affect the vertical migration and spatial distribution of phytoplankton are fundamental to aquatic ecology and biogeochemistry.

For motile phytoplankton (or more generally, any microswimmers), the interaction with the background flow occurs via advection due to the velocity field and rotation due to the velocity gradients, where the latter also involves body shape. This coupling between swimming, advection and body rotations has been studied in different contexts and shown to affect the spatial distributions of microswimmers and alter their vertical migration. In isotropic turbulence, microswimmers cluster and align nematically with fluid vorticity [1,2]. These results were extended, showing that the swimming direction also aligns in a polar way with fluid velocity due to correlations between the velocity field and velocity gradients along microswimmer trajectories, combined with swimming which breaks the fore–aft symmetry of relative motion with respect to the flow [3,4]. Microswimmers also show interesting spatial distributions in cellular flows [5–7] and isolated vortices [8–12] and non-trivial transport effects have been studied in microchannel flows [13–17]. Recent extensions of this research have begun to consider active control of transport by mechanisms such as optimal swimming strategies [18–20], biological responses to hydrodynamic cues [21–23] and mutual interactions of microswimmers in the presence of background flow [24].

Since upwards vertical migration towards well-lit waters is a common goal, many phytoplanktonic microswimmers exhibit gravitaxis, i.e. they tend to orient their swimming direction against gravity, owing to a bottom-heaviness within an uneven body mass distribution. When combined with flow-induced reorientations, this produces a phenomenon known as gyrotaxis [25]. Gyrotactic microswimmers display a plethora of behaviours in different flow conditions [26–28]. In turbulent flows, they form small-scale clusters, fractal distributions and sample vertical fluid velocities in shape-dependent ways [3,27,29–33]. Gyrotaxis can also lead to trapping in high shear [28,34,35], which is one mechanism for the formation of ‘thin phytoplankton layers’ commonly observed in the field [36,37]. When the fluid acceleration is comparable to the gravitational one, they respond to the total acceleration and can cluster in high vorticity regions [30].

Here, we consider the emerging topic of how microswimmers behave in flows with free-surface effects that are important for light-seeking phytoplankton [38–40]. This parallels recent work on passive particle transport in surface gravity waves [41–46]. In particular, we extend the previous work [40] that examined how microswimmers interact with a wavy background flow, to also consider gyrotactic and settling microswimmers within a more general flow configuration that includes a wind-driven shear superimposed on surface waves, a situation typically encountered in oceans [47]. Using a multiscale approach, we analyse the most general system of negatively buoyant gyrotactic swimmers with spheroidal body shapes in surface gravity waves with a wind-driven shear, followed by specific sub-cases that neglect certain aspects. In general, we find that both gyrotaxis and shear introduce new orientation effects that change the topology of microswimmer trajectories. Specifically, we observe trajectories where microswimmers are confined to a particular depth. By considering stability and observability of the trapping behaviour, we show how the depth at which microswimmers are trapped depends on the balance of different effects. For example, neutrally buoyant gyrotactic microswimmers in waves without shear oscillate about a depth where wave-induced re-orientation and gyrotactic re-orientation balance, whereas negatively buoyant gyrotactic microswimmers in the same flow field are attracted to a depth where the upwards swimming component (determined by the orientation dynamics) balances settling velocity. Overall, these trapping features of the system present new mechanisms that may contribute to the formation of thin phytoplankton layers in the ocean [36].

The rest of the paper is structured as follows. In §2, we describe the dynamics combining the effects of waves, linear shear and gyrotaxis on the swimmer’s mechanics. Section 3 focuses on specific sub-cases where certain effects are neglected in order to obtain interpretable analytical solutions. In §4, we provide a discussion where the results are placed into realistic oceanic and biological scenarios. Conclusions are provided in §5.

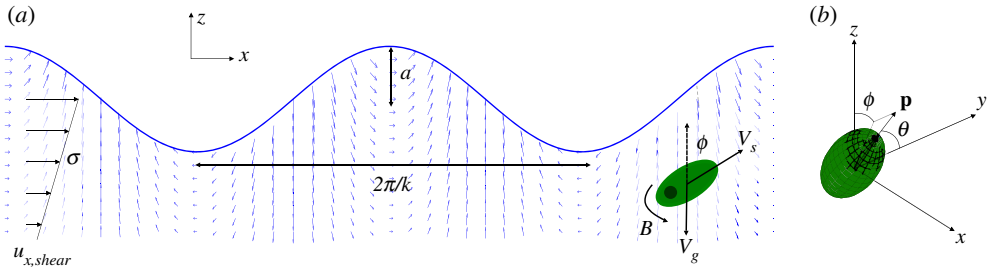


Figure 1. Definition sketch of the problem. (a) A prolate gyrotactic microswimmer swims with velocity V_s along its symmetry axis, settles with velocity V_g and re-orientates against gravity with characteristic timescale B . It interacts with a flow field induced by surface waves of amplitude a and wavenumber k , superposed on a linear shear with shear rate σ . (b) Definition of the orientation vector \mathbf{p} and associated angles ϕ and θ .

2. Mathematical model and multiple-scale analysis

We consider axisymmetric ellipsoidal microswimmers whose dynamics of position and orientation are described by (figure 1)

$$\left. \begin{aligned} \dot{\mathbf{x}} &= \mathbf{u} + V_s \mathbf{p} - V_g \mathbf{k} & (a) \\ \text{and} \quad \dot{\mathbf{p}} &= \Omega \mathbf{p} + \lambda [\mathbf{S} \mathbf{p} - (\mathbf{p}^T \mathbf{S} \mathbf{p}) \mathbf{p}] + \frac{1}{2B} [\mathbf{k} - (\mathbf{k} \cdot \mathbf{p}) \mathbf{p}]. & (b) \end{aligned} \right\} \quad (2.1)$$

In the first equation, which describes the microswimmer's velocity, there are three terms on the right-hand side: fluid transport, swimming and settling, respectively. The microswimmer moves with a constant swimming velocity V_s in the direction of its symmetry axis \mathbf{p} . The effect of negative buoyancy is taken into account by adding a constant vertical sinking velocity $\mathbf{v}_g = -V_g \mathbf{k}$, with \mathbf{k} being the unit vector in the vertical (z) direction. For the main body of this paper, we assume this simplified form of the settling velocity, neglecting the dependency of the settling velocity vector on the microswimmer orientation. Also, for the sake of brevity and because it captures the main phenomenology, in the main body of the paper, we limit the discussion to two-dimensional dynamics in which the microswimmer axis \mathbf{p} is restricted to the x - z plane and orientation is denoted by the angle measured relative to the vertical direction ($p_x = \sin \phi$; $p_z = \cos \phi$), as shown in figure 1. The full three-dimensional dynamics with a more complete model where the microswimmer settling velocity also depends on its orientation is considered in appendix B.

Equation (2.1b) describes the evolution of the particle's orientation: the first two terms come from the classic Jeffery's equation [48] for the rotation of a spheroid in a fluid due to local velocity gradients (in particular, $\Omega = (1/2)[\nabla \mathbf{u} - (\nabla \mathbf{u})^T]$ and $\mathbf{S} = (1/2)[\nabla \mathbf{u} + (\nabla \mathbf{u})^T]$ are the local rotation rate and strain rate tensors, respectively), and the last term describes the gyrotaxis for bottom-heavy microorganisms [27,49] which, in the absence of a flow, orient themselves against gravity with the characteristic re-orientation time B . The body shape of the swimmers is parametrized by $\lambda = (AR^2 - 1)/(AR^2 + 1)$, where AR is the aspect ratio of the body, i.e. the ratio of the diameter along the symmetry axis to the diameter perpendicular to that direction. Based on this definition $\lambda \in [-1, 1]$, with $\lambda > 0$ implying prolate swimmers and $\lambda < 0$ oblate ones. We focus on the former shape as it is the most common in aquatic microorganisms.

As for the fluid velocity field, we consider a monochromatic surface gravity wave travelling in the x -direction. Under the assumption of small wave amplitudes and deep water, the velocity

Table 1. Physical parameters and their non-dimensional forms.

parameter	description	dimensionless form
k	wavenumber	
ω	wave frequency	
λ	elongation (dimensionless)	
a	wave amplitude	$\alpha = ka$ (steepness)
V_s	swimming velocity	$\nu = V_s k / \omega$
V_g	settling velocity	$\nu_g = V_g k / \omega$
	sinking to swimming ratio	$r = \nu_g / \nu$
B	reorientation time	$\Psi = B\omega$
σ	shear	$\sigma' = \sigma / \omega$
β	linearized depth	$\beta' = \beta k$

field, which is incompressible and irrotational (i.e. $\Omega = 0$), is a solution of the Euler equations and given by

$$\left. \begin{aligned} u_x &= a\omega e^{kz} \cos(kx - \omega t) & (a) \\ u_z &= a\omega e^{kz} \sin(kx - \omega t), & (b) \end{aligned} \right\} \quad (2.2)$$

and

where $z \leq 0$ is the vertical domain (where $z = 0$ denotes the average surface position), a is the wave amplitude, k is the wavenumber and $\omega = \sqrt{gk}$ is the angular frequency (for further details, see for example [50, pp. 36–45]).

As a generalization of the simple monochromatic gravity wave, we introduce an additional shear velocity that represents the effect of wind on the surface velocity and, consequently, on the underlying fluid layers [47]. A simple model for the shear is given by an exponentially decaying velocity $u_{x,\text{shear}} = u_0 \exp(z/\beta)$ where β represents a characteristic depth [51–53]. In order to simplify the analytical treatment, we linearize the shear profile (for $z \geq -\beta$) as

$$u_{x,\text{shear}} = \sigma(\beta + z), \quad (2.3)$$

with $\sigma = u_0/\beta$ being the shear rate. In the approximation of linear waves and linear shear, we can then assume that the resulting general flow is obtained by a linear superposition of the wave and shear flows.

In what follows, all lengths and times are made dimensionless using k and ω , respectively. The resulting non-dimensional parameters are the *wave steepness* $\alpha = ak$, the *dimensionless shear rate* $\sigma' = \sigma/\omega$, the *dimensionless shear depth* $\beta' = \beta k$, the *swimming number* $\nu = kV_s/\omega$, the *settling number* $\nu_g = V_g k/\omega$ and the *stability number* $\Psi = B\omega$. Hereafter, we remove the primes for the sake of notational simplicity. The physical parameters used throughout the paper are summarized in table 1. Equation (2.1) takes the two-dimensional, dimensionless form

$$\left. \begin{aligned} \dot{x} &= \alpha e^z \cos(x - t) + \nu \sin \phi + \sigma(\beta + z), & (a) \\ \dot{z} &= \alpha e^z \sin(x - t) + \nu \cos \phi - \nu_g & (b) \\ \dot{\phi} &= \lambda \alpha e^z \cos(x - t + 2\phi) - \frac{1}{2\Psi} \sin \phi + \frac{\sigma}{2}(1 + \lambda \cos 2\phi). & (c) \end{aligned} \right\} \quad (2.4)$$

and

The range of validity of the model in equation (2.4) is $-\beta \leq z \leq 0$, where the lower limit is determined by the linearization of the shear and the upper limit is determined by the requirement that the swimmer remains below the average free surface position. In numerical simulations of (2.4), trajectories are stopped when z is outside the range $[-\beta, 0]$.

The dynamics of swimmers is characterized by fast oscillations at the surface wave frequency superposed with a slower trend at a longer timescale. Following the approach of [40,46], we use a multiple timescale expansion to remove the fast oscillations by introducing the slow timescale $T = \epsilon^2 t$. The magnitude of the parameters are assumed to scale as follows:

$$\alpha \rightarrow \epsilon \alpha; \quad \nu \rightarrow \epsilon^2 \nu; \quad \Psi^{-1} \rightarrow \epsilon^2 \Psi^{-1}; \quad \nu_g \rightarrow \epsilon^2 \nu_g; \quad \sigma \rightarrow \epsilon^2 \sigma. \quad (2.5)$$

The wave steepness α has to be small in order to guarantee the validity of the linear assumptions leading to (2.2), and is therefore assumed to be of $O(\epsilon)$. The fluid velocities, which are proportional to α in (2.4), are small compared to the wave phase speed ω/k and hence chosen to scale as $O(\epsilon)$. The swimmer parameters Ψ , ν and ν_g are chosen to scale as $O(\epsilon^2)$ since the swimmers are small and their dynamics is slow compared to the fluid motions. Finally, the shear in the upper ocean has a timescale that is typically much smaller than the wave period, and comparable to the reorientation time of microswimmers, and hence is chosen to scale as $O(\epsilon^2)$. We remark, however, that the scaling choices are dictated, as usual in multiple scale analysis [54], by the ultimate goal of eliminating secular terms via a solvability condition.

From the multiple timescale expansion, we obtain the following differential equations for the T -dependent slow variables (represented by upper-case letters) as a solvability condition at order ϵ^2 (see appendix A for details):

$$\left. \begin{aligned} \partial_T X &= \alpha^2 e^{2Z} + \nu \sin \Phi + \sigma(\beta + Z), & (a) \\ \partial_T Z &= \nu \cos \Phi - \nu_g & (b) \\ \text{and} \quad \partial_T \Phi &= \lambda \alpha^2 e^{2Z} [\cos(2\Phi) + \lambda] - \frac{1}{2\Psi} \sin(\Phi) + \frac{\sigma}{2}(1 + \lambda \cos 2\Phi). & (c) \end{aligned} \right\} \quad (2.6)$$

The first equation in (2.6) describes the horizontal motion and the first term represents the Stokes drift [55,56] which is always positive (in the direction of the waves) and can be enhanced or reduced by the other terms, as will be discussed in the following.

Remarkably, the dynamics of Z and Φ is independent of X , so we can study the two-dimensional system (Z, Φ) separately. In the plane (Z, Φ) , we find two fixed points (Z^+, Φ^+) and (Z^-, Φ^-) given by

$$\Phi^\pm = \pm \arccos(r), \quad (2.7)$$

where $r = \nu_g/\nu \geq 0$ is the ratio of the sinking speed and the swimming velocity, and

$$Z^\pm = \frac{1}{2} \ln \left[\frac{\pm \sqrt{1 - r^2} - \Psi \sigma (1 + \lambda(2r^2 - 1))}{2\Psi \lambda \alpha^2 (\lambda + 2r^2 - 1)} \right]. \quad (2.8)$$

The existence of the fixed points requires $r \leq 1$. Indeed if $r > 1$ (i.e. $\nu_g > \nu$) the swimmers sink and no fixed point can be reached. Depending on the stability of the corresponding solution, the existence of a fixed point can result in trapping of some swimmer trajectories at a finite depth from the free surface. This is the main finding of this work and it will be discussed in detail in the following sections.

3. Analysis of the fixed points and their stability

In this section, in order to make the results clearer, we study in detail the existence and the nature of the fixed points in (Φ, Z) in three different limits in which one or more ingredients of the model are disregarded.

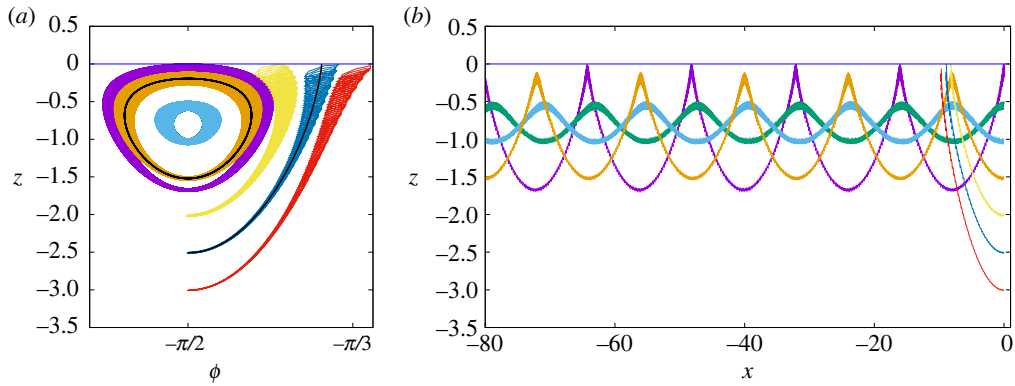


Figure 2. Numerical simulations for the pure gyrotactic case with $\alpha = 0.1$, $\lambda = 0.6$, $\nu = 0.01$ and $\Psi = 10^3$. Lines with different colours represent trajectories starting from $x = 0$ at different depths z and at a fixed initial orientation $\phi = -\pi/2$. The blue horizontal line is the average surface of the fluid. (a) Representation of the neutral fixed point ($\Phi^- = -\pi/2$, $Z^- = -0.7843$) in phase space. Black lines represent two examples of slow dynamics as average of fast oscillations. (b) Real space representation of the same trajectories. Waves propagate from left to right, while the swimmers swim in the opposite direction. The closed orbits in (a) correspond to swimmers trapped between two depths below the sea level.

(a) Pure gyrotaxis

We start by considering the case of a neutrally buoyant ($\nu_g = 0$, i.e. $r = 0$), gyrotactic swimmer ($\Psi < +\infty$) in the absence of shear ($\sigma = 0$). In this limit equations (2.6) simplify to

$$\left. \begin{aligned} \partial_T X &= \alpha^2 e^{2Z} + \nu \sin \Phi + \sigma(\beta + Z), & (a) \\ \partial_T Z &= \nu \cos \Phi - \nu_g & (b) \end{aligned} \right\} (2.6)$$

and

$$\partial_T \Phi = \lambda \alpha^2 e^{2Z} [\cos(2\Phi) + \lambda] - \frac{1}{2\Psi} \sin(\Phi) + \frac{\sigma}{2}(1 + \lambda \cos 2\Phi). \quad (c)$$

The fixed points (2.7)–(2.8) then become

$$\Phi^\pm = \pm \frac{\pi}{2}, \quad Z^\pm = \frac{1}{2} \ln \left[\frac{\pm 1}{2\Psi \lambda \alpha^2 (\lambda - 1)} \right], \quad (3.2)$$

and therefore we have only one real fixed point (Z^-, Φ^-). The stability analysis of this fixed point gives the eigenvalues $\eta_{1,2} = \pm i\sqrt{\nu/\Psi}$, meaning that the fixed point is neutrally stable. For the fixed point to be of physical relevance, i.e. to be below the water surface ($Z < 0$), the argument of the logarithm in equation (3.2) must be smaller than one, implying the observability condition

$$\Psi > \frac{1}{2\lambda(1-\lambda)\alpha^2}. \quad (3.3)$$

Since $\lambda = O(1)$ and, for linear waves, $\alpha \lesssim 0.1$ the above expression requires that $\Psi = B\omega = O(10^2)$. Therefore, depending on the wave frequency, the existence of a fixed point below the water surface may require a very long gyrotactic relaxation time B . We remark that large values of B have been observed for chains of gyrotactic cells (e.g. [57]). In figure 2, we show that the multiple-scale analysis accurately predicts the behaviour of the full dynamics obtained by numerical simulation of the original equations (2.4) with $\lambda = 0.6$, $\alpha = 0.1$, $\Psi = 10^3$ and $\nu = 0.01$ (code available at https://github.com/jeanluct/microgyro_code). Indeed, we observe a family of trajectories centred on the fixed point, the outermost of which extend roughly from the surface to a few times Z^- in depth. The orbits starting further away from the fixed point end up crossing the surface and cannot be consistently treated within our model.

We now consider the horizontal (X) dynamics. The first equation in (3.1) evaluated at the fixed point (3.2) gives the horizontal velocity

$$\partial_T X = \frac{1}{2\Psi\lambda(1-\lambda)} - v. \quad (3.4)$$

In general, the swimming direction (with speed v) is opposite to the Stokes drift (given by the first term in (3.4)). In the limit of large Ψ as required for observability, the Stokes drift is negligible and the horizontal motion is dominated by the swimming term. Under the observability condition (3.3), one can show that the swimming term in (3.4) dominates also when $v \geq \alpha^2$, as in the example shown in figure 2.

(b) Gyrotaxis combined with settling

We now consider the case of negatively buoyant ($v_g > 0$) gyrotactic swimmers ($\Psi < +\infty$), still in the absence of shear ($\sigma = 0$). The equations for the slow variables are still given by (3.1) with the equation for Z modified to $\partial_T Z = v \cos \Phi - v_g$, so that the fixed points become $\Phi^\pm = \pm \arccos r$ (as in (2.7)) and

$$Z^\pm = \frac{1}{2} \ln \left[\frac{\pm \sqrt{1-r^2}}{2\Psi\lambda\alpha^2(\lambda + 2r^2 - 1)} \right], \quad (3.5)$$

as easily derived from (2.8) for $\sigma = 0$. The domain of existence of the fixed points is

$$(\Phi^-, Z^-) \in \mathbb{R} \Leftrightarrow 0 < r < \sqrt{\frac{1}{2}(1-\lambda)} \quad (3.6a)$$

and

$$(\Phi^+, Z^+) \in \mathbb{R} \Leftrightarrow \sqrt{\frac{1}{2}(1-\lambda)} < r < 1. \quad (3.6b)$$

The eigenvalues associated with the fixed points (Φ^-, Z^-) are

$$\eta_{1,2} = -\frac{r(3-2r^2+\lambda) \pm \sqrt{r^2(3-2r^2+\lambda)^2 - 16\Psi(1-r^2)(2r^2-1+\lambda)^2}}{4\Psi(2r^2-1+\lambda)}. \quad (3.7)$$

It is easily checked that the eigenvalues always have a positive real part and therefore the fixed point (Φ^-, Z^-) is unstable. Clearly, in the limit $r = 0$, the eigenvalues become imaginary and we recover the results of §3a.

The eigenvalues associated with the fixed point (Φ^+, Z^+) are still given by (3.7) but, in this case, in the domain of existence the real part of the eigenvalues is negative and therefore (Φ^+, Z^+) is stable. The observability condition (i.e. $Z^+ < 0$) is more complicated than in the previous case since it involves a combination of the parameters Ψ and r , and will be discussed in the context of numerical simulations in §4 below. Figure 3 shows how several trajectories converge, asymptotically oscillating around a mean depth Z^+ .

As for the horizontal dynamics, once the attractive fixed point (Φ^+, Z^+) is reached, the motion is given by

$$\partial_T X = \frac{\sqrt{1-r^2}}{2\Psi\lambda(\lambda-1+2r^2)} + v\sqrt{1-r^2}. \quad (3.8)$$

In the domain of existence of the fixed point, both terms in (3.8) are positive, and therefore in this case the Stokes drift is enhanced by swimming.

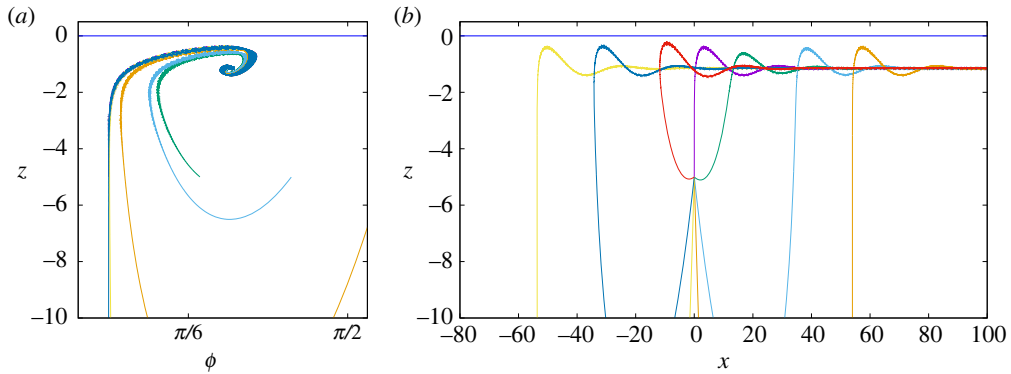


Figure 3. Attractive fixed point in the gyrotactic case with a settling velocity. The parameter values $\lambda = 0.6$, $\Psi = 10^3$, $r = 0.7$ (i.e. $\nu = 0.01$ and $\nu_g = 0.007$) and $\alpha = 0.1$ result in $Z^+ = -1.14$. Lines with different colours represent trajectories starting from $x = 0$ at a fixed depth $z = -5$ and different orientations in $\phi \in [0, 2\pi]$. All trajectories converge to each other. (a) Dynamics around the fixed point in phase space. (b) Corresponding real space representation. Both the waves' propagation and swimming are from left to right.

(c) Pure shear

We now consider a neutrally buoyant ($\nu_g = 0$), non-gyrotactic swimmer ($\Psi \rightarrow \infty$) in a velocity field characterized by waves with a linear shear ($\sigma \neq 0$). From (2.6), the equations are

$$\left. \begin{aligned} \partial_T X &= \alpha^2 e^{2Z} + \nu \sin \Phi + \sigma(\beta + Z), & (a) \\ \partial_T Z &= \nu \cos \Phi & (b) \end{aligned} \right\} \quad (3.9)$$

and

$$\partial_T \Phi = \lambda \alpha^2 e^{2Z} [\cos(2\Phi) + \lambda] + \frac{\sigma}{2} (1 + \lambda \cos 2\Phi). \quad (c)$$

The system has two fixed points, which can be obtained from (2.8) for $r = 0$ after taking the limit $\Psi \rightarrow \infty$, given by $\Phi^\pm = \pm\pi/2$ and

$$Z^* = \frac{1}{2} \ln \left[\frac{\sigma}{2\lambda\alpha^2} \right]. \quad (3.10)$$

The observability condition $Z^* < 0$ in the existence domain requires that

$$0 < \sigma \leq 2\lambda\alpha^2. \quad (3.11)$$

The stability analysis for the fixed points leads to the eigenvalues $\eta_{1,2} = \pm i\sqrt{\nu\sigma(1-\lambda)}$ for $(-\pi/2, Z^*)$, i.e. a neutral fixed point, and $\eta_{1,2} = \pm\sqrt{\nu\sigma(1-\lambda)}$ for $(+\pi/2, Z^*)$, i.e. an unstable fixed point. Thus, the dynamics in the plane (Φ, Z) is qualitatively similar to the case of pure gyrotaxis discussed in §3a, as shown in figure 4 (to be compared with figure 2). We remark that for typical values $\lambda = 0.6$ and $\alpha = 0.1$, the observability condition becomes $\sigma \leq 0.012$ which, as we will see, is a number compatible with values observed in the ocean.

The horizontal dynamics at the neutral fixed point is in this case given by

$$\partial_T X = \frac{\sigma}{2\lambda} - \nu + \sigma(\beta + Z^*), \quad (3.12)$$

with Z^* given by (3.10). The Stokes drift (first term in (3.12)) is proportional to the shear. Since in the model of the shear we assume $|Z| \leq \beta$, the last term is also positive, while the swimming contribution is negative, i.e. opposite to the direction of waves and the shear. The resulting horizontal motion depends on the parameters and can be either upstream or downstream as in figure 4. We remark that this result is consistent with the multiple scale analysis in which ν and σ are both second-order terms: their relative magnitude controls the sign of the horizontal velocity.

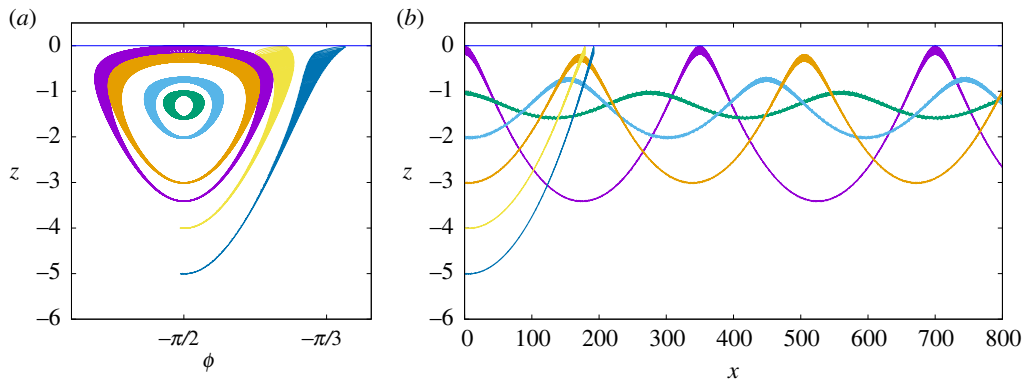


Figure 4. Fixed point in the case with shear only. We use $\sigma = 10^{-3}$, $\beta = 100$, $\lambda = 0.6$, $\alpha = 0.1$ and $\nu = 0.01$, which results in $Z \simeq -1.24$. Lines with different colours represent trajectories starting from $x = 0$ at different depths with a fixed initial orientation $\phi = -\pi/2$. (a) Dynamics around the fixed point in the phase space representation. (b) Corresponding trajectories in real space. The waves' direction is from left to right. The mean velocity is left to right despite the swimmer's upstream orientation, as in this particular case transport is dominated by shear.

4. Discussion

The analysis in the previous sections has been carried out in dimensionless variables. We now discuss the applicability of our results in the context of realistic values for the dimensional parameters. Figure 5 summarizes the different cases discussed in the paper.

The particle elongation and the wave steepness are fixed, respectively, to $\lambda = 0.6$, which corresponds to $AR = 2$ and are in the range of typical values for gyrotactic microorganisms [35]. The wave steepness, $\alpha = 0.1$, is a reasonable value for linear waves as used in our model. The linear wave model is derived under a number of approximations. For the case of deep water (as assumed here), the main limit of validity of the theory is the upper limit of α (e.g. the waves are expected to break for $\alpha = 1/7$ according to [58]). Thus $\alpha = 0.1$ is at the border of values above which second-order terms in the wave theory become important and the linear theory is no longer valid.

All plots refer to the analytical solutions for the depth Z^* of the fixed point (stable or neutral) varying one or more parameters in the different limits discussed in §3. The range of wavenumbers k is chosen to be in the range of values typical of wavelengths encountered in the ocean [59]. Recall that physically one must have $Z^* < 0$, which corresponds to the observability condition $z^* < -a$ in dimensional form with an oscillating surface.

The pure gyrotactic case is described in figure 5a, where the depth of the fixed point in equation (3.2) is plotted as a function of the wavenumber and the gyrotactic orientation time B . The plot shows that, for typical values of k , negative values of z^* are obtained for large values of B , outside the typical range (of a few seconds) cited in the literature [21,60]. For example, the case discussed in figure 2 with $k = 1 \text{ m}^{-1}$ corresponds to $B \simeq 300 \text{ s}$ and a depth of the fixed point $z^* \simeq -0.8 \text{ m}$. In this case, the Stokes drift velocity in (3.4) is $O(1) \text{ cm s}^{-1}$, much larger than typical swimming velocities. Thus, there is no trapping behaviour for neutrally buoyant gyrotactic organisms swimming in waves without shear with realistic re-orientation times.

We now consider the case of sinking gyrotactic microswimmers. Figure 5b displays the depth z^* of the fixed point as a function of B and $r = V_g/V_s$ at fixed wavenumber $k = 0.1 \text{ m}^{-1}$, whereas figure 5c shows the depth of the fixed point as a function of k for two values of B at fixed $r = 0.9$. Remarkably, the position of the fixed point is non-monotonic in k , and the position of the minimum value depends on the value of B . In figure 5c rather large values of B were chosen as examples, compatible with those observed in chain-forming organisms [57] and larger than the ones expected for single cells. Even considering those large values of B , a negative value

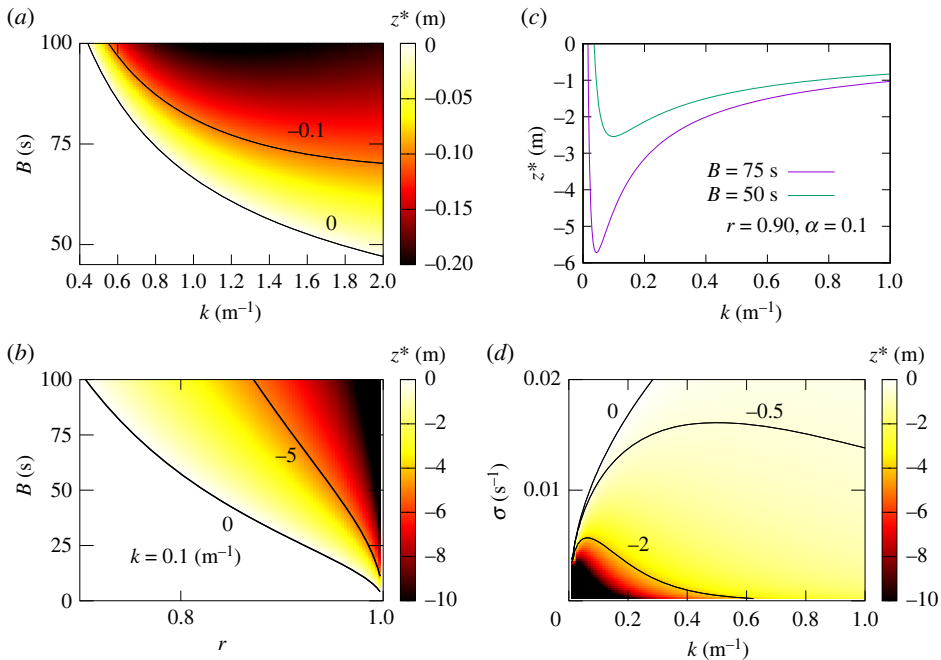


Figure 5. Depth of the fixed points as a function of the parameters in the different regimes for $\alpha = 0.1$ and $\lambda = 0.6$. (a) Pure gyrotactic case (§3a). Negative values of z^* require large values of B . (b) Gyrotactic and settling case (§3b) with wavenumber $k = 0.1 \text{ m}^{-1}$. Large negative values of z^* are obtained for large values of B and r close to one. (c) Gyrotactic and settling case (as in (b)) with $r = 0.9$ as a function of k . The depth is a non-monotonic function of k with a absolute minimum (maximum depth) that is dependent on B : greater B implies deeper depth (according to [57] very high values of B are observed for chains of phytoplankton). (d) Shear case (§3c) as a function of wavenumber and shear intensity.

of z^* requires $r = O(1)$, i.e. a settling velocity V_g close to the swimming speed V_s . This is not common in swimming microorganisms, since motility is often assumed to evolve as a way to escape sinking through the water column. For example, *Chlamydomonas reinhardtii* swims with speed $50\text{--}70 \mu\text{m s}^{-1}$ while its sedimentation speed is only $2.5 \mu\text{m s}^{-1}$ [60].

Finally, we discuss the case of swimmers in waves with a shear, in the absence of gyrotaxis and sedimentation. Figure 5d shows the depth of the fixed point z^* as a function of the wavenumber k and the shear rate σ . The observability condition in this case requires small values of the shear rate $\sigma \lesssim 10^{-2} \text{ s}^{-1}$ which are common in the ocean [61]. In this case, confinement at a few metres below the surface is compatible with realistic values of the parameters. Using the parameters of figure 4, with a wavenumber $k = 0.2 \text{ m}^{-1}$, the horizontal motion (3.12) is dominated by the shear term and the swimmer moves downstream.

5. Conclusion

In this paper, we have studied the dynamics of elongated microorganisms swimming in the flow produced by water waves and a linear shear. We have investigated in detail how the interplay of swimming and flow leads to trapping of the microswimmers below the water surface. The analysis has been done by exploiting a multiple scale analysis, extending the work in [40,46], complemented by numerical simulations. In general, our results demonstrate that the combination of swimming and flow (and/or gravity) can produce trapping but this process depends on the details of the physical and biological parameters. In particular, we have found that the presence of a shear (in combination with waves) close to the surface is essential to produce confinement with realistic values of the parameters. This is a promising finding with regards to

how the mechanisms discussed above could lead to the production of ‘thin phytoplankton layers’ since wind-generated shear will often accompany locally generated waves.

Future investigations should consider more realistic models of the microswimmers (e.g. including some randomness in the swimmer behaviour) and of the velocity field, beyond the kinematic model for linear waves, as for example in the case of nonlinear waves where fluid accelerations may also become comparable to gravity requiring a more complete model of gyrotaxis [30]. Furthermore, it would be very interesting to study the problem of swimmer–water wave interaction by means of laboratory experiments with real microswimmers to see the degree of agreement with this simple model.

Data accessibility. The numerical code used for the simulations is available at https://github.com/jeanluct/microgyro_code.

Declaration of AI use. We have not used AI-assisted technologies in creating this article.

Authors’ contributions. F.M.V.: conceptualization, formal analysis, investigation, software, visualization, writing—original draft, writing—review and editing; N.P.: conceptualization, formal analysis, methodology, writing—original draft, writing—review and editing; G.B.: conceptualization, methodology, writing—original draft, writing—review and editing; M.C.: conceptualization, methodology, writing—original draft, writing—review and editing; J.-L.T.: conceptualization, methodology, supervision, writing—original draft, writing—review and editing; F.D.L.: conceptualization, methodology, supervision, writing—original draft, writing—review and editing.

All authors gave final approval for publication and agreed to be held accountable for the work performed therein.

Conflict of interest declaration. We declare we have no competing interests.

Funding. N.P. acknowledges support from the US National Science Foundation (CBET-2211704 and OCE-2048676). F.M.V., G.B. and F.D.L. acknowledge support by the Departments of Excellence grant (MIUR).

Acknowledgements. F.M.V., G.B. and F.D.L. are indebted to M. Onorato for numerous fruitful discussions.

Appendix A. Multiple scale analysis

We start from (2.4) with parameters rescaled according to (2.5) and multiple times ($t, T = \epsilon^2 t$)

$$\left. \begin{aligned} \partial_t x + \epsilon^2 \partial_T x &= \epsilon \alpha e^z \cos(x - t) + \epsilon^2 \nu \sin \phi + \epsilon^2 \sigma (\beta + z), \\ \partial_t z + \epsilon^2 \partial_T z &= \epsilon \alpha e^z \sin(x - t) + \epsilon^2 \nu \cos \phi - \epsilon^2 \nu_g \\ \text{and } \partial_t \phi + \epsilon^2 \partial_T \phi &= \lambda \epsilon \alpha e^z \cos(x - t + 2\phi) - \epsilon^2 \frac{1}{2\psi} \sin \phi + \epsilon^2 \frac{\sigma}{2} (1 + \lambda \cos 2\phi), \end{aligned} \right\} \quad (\text{A } 1)$$

together with a perturbative expansion of the variables [54]:

$$\left. \begin{aligned} x &= x_0 + \epsilon x_1 + \epsilon^2 x_2 + \dots, \\ z &= z_0 + \epsilon z_1 + \epsilon^2 z_2 + \dots \\ \text{and } \phi &= \phi_0 + \epsilon \phi_1 + \epsilon^2 \phi_2 + \dots \end{aligned} \right\} \quad (\text{A } 2)$$

At order zero, ϵ^0 , (A 1) gives

$$\left. \begin{aligned} \partial_t x_0 &= 0 \implies x_0 = X(T), \\ \partial_t z_0 &= 0 \implies z_0 = Z(T) \\ \text{and } \partial_t \phi_0 &= 0 \implies \phi_0 = \Phi(T), \end{aligned} \right\} \quad (\text{A } 3)$$

i.e. zero-order solutions are function of the slow time T only.

At the order ϵ^1 , we have

$$\left. \begin{aligned} \partial_t x_1 &= \alpha e^Z \cos(X - t), \\ \partial_t z_1 &= \alpha e^Z \sin(X - t) \\ \text{and} \quad \partial_t \phi_1 &= \alpha \lambda e^Z \cos(X + 2\Phi - t). \end{aligned} \right\} \quad (\text{A } 4)$$

Note that the integral on t over $[0, 2\pi]$ of the right-hand side of each equation (A 4) vanishes (which is the solvability condition) and therefore the solutions are [40]

$$\left. \begin{aligned} x_1 &= -\alpha e^Z \sin(X - t), \\ z_1 &= \alpha e^Z \cos(X - t) \\ \text{and} \quad \phi_1 &= -\alpha \lambda e^Z \sin(X + 2\Phi - t). \end{aligned} \right\} \quad (\text{A } 5)$$

Finally, at the order ϵ^2 , we have

$$\left. \begin{aligned} \partial_t x_2 + \partial_T X &= \alpha^2 e^{2Z} + \nu \sin \Phi + \sigma(\beta + Z), \\ \partial_t z_2 + \partial_T Z &= \nu \cos \Phi - \nu_g \\ \text{and} \quad \partial_t \phi_2 + \partial_T \Phi &= \alpha^2 \lambda e^{2Z} [\cos(2\Phi) + 2\lambda \sin^2(X - t + 2\Phi)] \\ &\quad - \frac{1}{2\Psi} \sin \Phi + \frac{\sigma}{2} (1 + \lambda \cos 2\Phi). \end{aligned} \right\} \quad (\text{A } 6)$$

At this order, by averaging (A 6) over one period, we obtain the non-trivial solvability conditions (2.6). Full details for analogous calculations are available in [40,46].

Appendix B. Three-dimensional model with orientation-dependent settling

We now introduce two extensions which improve the mathematical model. The first one is to consider a three-dimensional model, in which the orientation of the swimmers is parametrized by the two angles (θ, ϕ) and therefore

$$\mathbf{p} = (\sin \theta \sin \phi, \cos \theta, \sin \theta \cos \phi). \quad (\text{B } 1)$$

The second modification is a more realistic model for the settling velocity which depends on the orientation of the ellipsoidal body:

$$\mathbf{v}_g = -v_s [\hat{\mathbf{k}} + (v_{sr} - 1)(\hat{\mathbf{k}} \cdot \mathbf{p})\mathbf{p}], \quad (\text{B } 2)$$

where v_s is the settling velocity in quiescent fluid in the highest drag orientation (i.e. symmetry axis perpendicular to gravity for prolate spheroids and symmetry axis parallel to gravity for oblate spheroids), and v_{sr} is the relative increment of this velocity in the case of lowest drag orientation (and thus $v_{sr} > 1$). For prolate spheroids, we have (e.g. [62])

$$v_s = \frac{3S\sqrt{(1/\lambda) - 1}}{32\lambda} \left[2\sqrt{\lambda(1 + \lambda)} + \sqrt{2}(5\lambda - 1) \operatorname{arcsinh} \left(\sqrt{\frac{1 + \lambda}{1 - \lambda}} - 1 \right) \right] \quad (\text{B } 3)$$

and

$$v_{sr} = - \frac{2\sqrt{2\lambda(1 + \lambda)} + 2(3\lambda + 1) \operatorname{arcsinh} \left(\sqrt{\frac{1 + \lambda}{1 - \lambda}} - 1 \right)}{\sqrt{2\lambda(1 + \lambda)} + (5\lambda - 1) \operatorname{arcsinh} \left(\sqrt{\frac{1 + \lambda}{1 - \lambda}} - 1 \right)}, \quad (\text{B } 4)$$

where $S = (\rho_p - \rho)d_p^2 g k / 18\mu\omega$ and μ is the dynamic viscosity, ρ is the fluid density, ρ_p is the particle's density, d_p is the particle diameter. Note that both v_s and v_{sr} are dimensionless.

The complete model reads

$$\left. \begin{aligned} \dot{x} &= \alpha e^z \cos(x-t) + v \sin \phi \sin \theta - v_s(v_{sr} - 1) \cos \phi \sin \phi \sin^2 \theta, & (a) \\ \dot{y} &= v \cos \theta - v_s(v_{sr} - 1) \cos \phi \cos \theta \sin \theta, & (b) \\ \dot{z} &= \alpha e^z \sin(x-t) + v \cos \phi \sin \theta - v_s[1 + (v_{sr} - 1) \cos^2 \phi \sin^2 \theta], & (c) \\ \dot{\phi} &= \lambda \alpha e^z \cos(x-t + 2\phi) - \frac{1}{2\Psi} \frac{\sin \phi}{\sin \theta} & (d) \end{aligned} \right\} \quad (B5)$$

and

$$\dot{\theta} = \lambda \alpha e^z \cos \theta \sin \theta \sin(x-t + 2\phi) + \frac{1}{2\Psi} \cos \theta \cos \phi. \quad (e)$$

It is again possible to obtain the slow-time equations using a multiple scale analysis. Neglecting the equations for X and Y , that are independent of the others, one obtains

$$\left. \begin{aligned} \partial_T Z &= v \cos \Phi \sin \Theta - v_s[1 + (v_{sr} - 1) \cos^2 \Phi \sin^2 \Theta], & (a) \\ \partial_T \Phi &= \lambda \alpha^2 e^{2Z} (\lambda + \cos(2\Phi)) - \frac{1}{2\Psi} \frac{\sin \Phi}{\sin \Theta} & (b) \end{aligned} \right\} \quad (B6)$$

and

$$\partial_T \Theta = \lambda \alpha^2 e^{2Z} \cos \Theta \sin \Theta \sin(2\Phi) + \frac{1}{2\Psi} \cos \Theta \cos \Phi. \quad (c)$$

From the third equation, we note that a solution is $\cos \theta = 0$ and so $\theta = \pi/2$. Based on the analysis of the two-dimensional case, we expect that a pair of fixed points is on the xz -plane. We remark that $\theta = \pi/2$ is also the stable orientation for neutrally buoyant, non-swimmers [46]. Using $\theta = \pi/2$ in (B6), we obtain the equation for the fixed points as

$$\left. \begin{aligned} v \cos \Phi - v_s[1 + (v_{sr} - 1) \cos^2 \Phi] &= 0 & (a) \\ \lambda \alpha^2 e^{2Z} (\lambda + \cos(2\Phi)) - \frac{1}{2\Psi} \sin \Phi &= 0. & (b) \end{aligned} \right\} \quad (B7)$$

and

The first equation gives two real solutions for the angle Φ

$$\Phi^\pm = \pm \arccos(A), \quad \text{where } A = \frac{1 - \sqrt{1 - 4q^2(v_{sr} - 1)}}{2q(v_{sr} - 1)} \quad (B8)$$

and $q = v_s/v$. The associated values of Z are

$$Z^\pm = \frac{1}{2} \ln \left(\pm \frac{\sqrt{1 - A^2}}{2\Psi \lambda \alpha^2 (\lambda - 1 + 2A^2)} \right). \quad (B9)$$

The existence domain and the physical observability condition (i.e. whether $Z < 0$) of these fixed points are not trivial, but it can be shown that they never coexist in the same range of parameters and, where they exist, they are both negative (i.e. below the sea level, thus observable).

We can conclude that the three-dimensional case is a natural extension of the two-dimensional one. Indeed, despite the different form of the settling velocity, the fixed points qualitatively agree with the results in §3b. One can also note that in the formal limit $v_{sr} \rightarrow 1$ (B9) reduces to (3.5) once the identification $v_g = v_s$ is made and v_{sr} and v_g are considered as independent on λ .

References

1. Zhan C, Sardina G, Lushi E, Brandt L. 2013 Accumulation of motile elongated microorganisms in turbulence. *J. Fluid Mech.* **739**, 22–36. (doi:10.1017/jfm.2013.608)
2. Pujara N, Koehl M, Variano E. 2018 Rotations and accumulation of ellipsoidal microswimmers in isotropic turbulence. *J. Fluid Mech.* **838**, 356–368. (doi:10.1017/jfm.2017.912)
3. Borgnino M, Gustavsson K, De Lillo F, Boffetta G, Cencini M, Mehlig B. 2019 Alignment of nonspherical active particles in chaotic flows. *Phys. Rev. Lett.* **123**, 138003. (doi:10.1103/PhysRevLett.123.138003).

4. Borgnino M, Boffetta G, Cencini M, De Lillo F, Gustavsson K. 2022 Alignment of elongated swimmers in a laminar and turbulent Kolmogorov flow. *Phys. Rev. Fluids* **7**, 074603. (doi:10.1103/PhysRevFluids.7.074603)
5. Torney C, Neufeld Z. 2007 Transport and aggregation of self-propelled particles in fluid flows. *Phys. Rev. Lett.* **99**, 078101. (doi:10.1103/PhysRevLett.99.078101)
6. Khurana N, Blawdziewicz J, Ouellette NT. 2011 Reduced transport of swimming particles in chaotic flow due to hydrodynamic trapping. *Phys. Rev. Lett.* **106**, 198104. (doi:10.1103/PhysRevLett.106.198104)
7. Khurana N, Ouellette NT. 2012 Interactions between active particles and dynamical structures in chaotic flow. *Phys. Fluids* **24**, 091902. (doi:10.1063/1.4754873)
8. Sokolov A, Aranson IS. 2016 Rapid expulsion of microswimmers by a vortical flow. *Nat. Commun.* **7**, 11114. (doi:10.1038/ncomms11114)
9. Berman SA, Buggeln J, Brantley DA, Mitchell KA, Solomon TH. 2021 Transport barriers to self-propelled particles in fluid flows. *Phys. Rev. Fluids* **6**, L012501. (doi:10.1103/PhysRevFluids.6.L012501)
10. Berman SA, Mitchell KA. 2020 Trapping of swimmers in a vortex lattice. *Chaos* **30**, 063121. (doi:10.1063/5.0005542)
11. Arguedas-Leiva J, Wilczek M. 2020 Microswimmers in an axisymmetric vortex flow. *New J. Phys.* **22**, 053051. (doi:10.1088/1367-2630/ab776f)
12. Tanasijević I, Lauga E. 2022 Microswimmers in vortices: dynamics and trapping. *Soft Matter* **18**, 8931–8944. (doi:10.1039/D2SM00907B)
13. Rusconi R, Guasto JS, Stocker R. 2014 Bacterial transport suppressed by fluid shear. *Nat. Phys.* **10**, 212–217. (doi:10.1038/nphys2883)
14. Zöttl A, Stark H. 2012 Nonlinear dynamics of a microswimmer in Poiseuille flow. *Phys. Rev. Lett.* **108**, 218104. (doi:10.1103/PhysRevLett.108.218104)
15. Zöttl A, Stark H. 2013 Periodic and quasiperiodic motion of an elongated microswimmer in Poiseuille flow. *Eur. Phys. J. E* **36**, 4. (doi:10.1140/epje/i2013-13004-5)
16. Junot G, Figueroa-Morales N, Darnige T, Lindner A, Soto R, Auradou H, Clément E. 2019 Swimming bacteria in Poiseuille flow: the quest for active Bretherton-Jeffery trajectories. *EPL* **126**, 44003. (doi:10.1209/0295-5075/126/44003)
17. Bearon RN, Hazel AL. 2015 The trapping in high-shear regions of slender bacteria undergoing chemotaxis in a channel. *J. Fluid Mech.* **771**, R3. (doi:10.1017/jfm.2015.198)
18. Colabrese S, Gustavsson K, Celani A, Biferale L. 2017 Flow navigation by smart microswimmers via reinforcement learning. *Phys. Rev. Lett.* **118**, 158004. (doi:10.1103/PhysRevLett.118.158004)
19. Qiu J, Mousavi N, Gustavsson K, Xu C, Mehlig B, Zhao L. 2022 Navigation of microswimmers in steady flow: the importance of symmetries. *J. Fluid Mech.* **932**, A10. (doi:10.1017/jfm.2021.978)
20. Monthiller R, Loisy A, Koehl MA, Favier B, Eloy C. 2022 Surfing on turbulence: a strategy for planktonic navigation. *Phys. Rev. Lett.* **129**, 064502. (doi:10.1103/PhysRevLett.129.064502)
21. Sengupta A, Carrara F, Stocker R. 2017 Phytoplankton can actively diversify their migration strategy in response to turbulent cues. *Nature* **543**, 555–558. (doi:10.1038/nature21415)
22. Du Clos KT, Karp-Boss L, Villareal TA, Gemmill BJ. 2019 *Coscinodiscus wailesii* mutes unsteady sinking in dark conditions. *Biol. Lett.* **15**, 20180816. (doi:10.1098/rsbl.2018.0816)
23. Pujara N, Clos KTD, Ayres S, Variano EA, Karp-Boss L. 2021 Measurements of trajectories and spatial distributions of diatoms (*Coscinodiscus* spp.) at dissipation scales of turbulence. *Exp. Fluids* **62**, 149. (doi:10.1007/s00348-021-03240-5)
24. Breier RE, Lalescu CC, Waas D, Wilczek M, Mazza MG. 2018 Emergence of phytoplankton patchiness at small scales in mild turbulence. *Proc. Natl Acad. Sci. USA* **115**, 12112–12117. (doi:10.1073/pnas.1808711115)
25. Kessler JO. 1985 Hydrodynamic focusing of motile algal cells. *Nature* **313**, 218–220. (doi:10.1038/313218a0)
26. Thorn GJ, Bearon RN. 2010 Transport of spherical gyrotactic organisms in general three-dimensional flow fields. *Phys. Fluids* **22**, 041902. (doi:10.1063/1.3381168)
27. Cencini M, Boffetta G, Borgnino M, De Lillo F. 2019 Gyrotactic phytoplankton in laminar and turbulent flows: a dynamical systems approach. *Eur. Phys. J. E* **42**, 31. (doi:10.1140/epje/i2019-11792-0)
28. Bearon RN, Durham WM. 2023 Elongation enhances migration through hydrodynamic shear. *Phys. Rev. Fluids* **8**, 033101. (doi:10.1103/PhysRevFluids.8.033101)

29. Durham WM, Climent E, Barry M, De Lillo F, Boffetta G, Cencini M, Stocker R. 2013 Turbulence drives microscale patches of motile phytoplankton. *Nat. Commun.* **4**, 2148. (doi:10.1038/ncomms3148)
30. De Lillo F, Cencini M, Durham WM, Barry M, Stocker R, Climent E, Boffetta G. 2014 Turbulent fluid acceleration generates clusters of gyrotactic microorganisms. *Phys. Rev. Lett.* **112**, 044502. (doi:10.1103/PhysRevLett.112.044502)
31. Gustavsson K, Berglund F, Jonsson P, Mehlig B. 2016 Preferential sampling and small-scale clustering of gyrotactic microswimmers in turbulence. *Phys. Rev. Lett.* **116**, 108104. (doi:10.1103/PhysRevLett.116.108104)
32. Liu Z, Jiang L, Sun C. 2022 Accumulation and alignment of elongated gyrotactic swimmers in turbulence. *Phys. Fluids* **34**, 033303. (doi:10.1063/5.0083802)
33. Qiu J, Marchioli C, Zhao L. 2022 A review on gyrotactic swimmers in turbulent flows. *Acta Mech. Sin.* **38**, 722323. (doi:10.1007/s10409-022-22323-x)
34. Durham WM, Kessler JO, Stocker R. 2009 Disruption of vertical motility by shear triggers formation of thin phytoplankton layers. *Science* **323**, 1067–1070. (doi:10.1126/science.1167334)
35. Barry MT, Rusconi R, Guasto JS, Stocker R. 2015 Shear-induced orientational dynamics and spatial heterogeneity in suspensions of motile phytoplankton. *J. R. Soc. Interface* **12**, 20150791. (doi:10.1098/rsif.2015.0791)
36. Durham WM, Stocker R. 2012 Thin phytoplankton layers: characteristics, mechanisms, and consequences. *Annu. Rev. Mar. Sci.* **4**, 177–207. (doi:10.1146/annurev-marine-120710-100957)
37. Wheeler JD, Secchi E, Rusconi R, Stocker R. 2019 Not just going with the flow: the effects of fluid flow on bacteria and plankton. *Annu. Rev. Cell Dev. Biol.* **35**, 213–237. (doi:10.1146/annurev-cellbio-100818-125119)
38. Marchioli C, Bhatia H, Sardina G, Brandt L, Soldati A. 2019 Role of large-scale advection and small-scale turbulence on vertical migration of gyrotactic swimmers. *Phys. Rev. Fluids* **4**, 124304. (doi:10.1103/PhysRevFluids.4.124304)
39. Mashayekhpour M, Marchioli C, Lovecchio S, Lay EN, Soldati A. 2019 Wind effect on gyrotactic micro-organism surfacing in free-surface turbulence. *Adv. Water Resour.* **129**, 328–337. (doi:10.1016/j.advwatres.2017.09.001)
40. Ma K, Pujara N, Thiffeault JL. 2022 Reaching for the surface: spheroidal microswimmers in surface gravity waves. *Phys. Rev. Fluids* **7**, 014310. (doi:10.1103/PhysRevFluids.7.014310)
41. Santamaria F, Boffetta G, Afonso MM, Mazzino A, Onorato M, Pugliese D. 2013 Stokes drift for inertial particles transported by water waves. *Europhys. Lett.* **102**, 14003. (doi:10.1209/0295-5075/102/14003)
42. DiBenedetto MH, Ouellette NT. 2018 Preferential orientation of spheroidal particles in wavy flow. *J. Fluid Mech.* **856**, 850–869. (doi:10.1017/jfm.2018.738)
43. Bremer TS, Whittaker C, Calvert R, Raby A, Taylor PH. 2019 Experimental study of particle trajectories below deep-water surface gravity wave groups. *J. Fluid Mech.* **879**, 168–186. (doi:10.1017/jfm.2019.584)
44. Calvert R, McAllister M, Whittaker C, Raby A, Borthwick A. 2021 A mechanism for the increased wave-induced drift of floating marine litter. *J. Fluid Mech.* **915**, A73. (doi:10.1017/jfm.2021.72)
45. DiBenedetto MH, Clark LK, Pujara N. 2022 Enhanced settling and dispersion of inertial particles in surface waves. *J. Fluid Mech.* **936**, A38. (doi:10.1017/jfm.2022.95)
46. Pujara N, Thiffeault JL. 2023 Wave-averaged motion of small particles in surface gravity waves: effect of particle shape on orientation, drift, and dispersion. *Phys. Rev. Fluids* **8**, 074801. (doi:10.1103/PhysRevFluids.8.074801)
47. Shemdin OH. 1972 Wind-generated current and phase speed of wind waves. *J. Phys. Oceanogr.* **2**, 411–419. (doi:10.1175/1520-0485(1972)002<0411:WGCAPS>2.0.CO;2)
48. Jeffery GB. 1922 The motion of ellipsoidal particles immersed in a viscous fluid. *Proc. R. Soc. Lond.* **102**, 161–179. (doi:10.1098/rspa.1922.0078)
49. Pedley TJ, Kessler JO. 1987 The orientation of spheroidal microorganisms swimming in a flow field. *Proc. R. Soc. Lond. B* **231**, 47–70. (doi:10.1098/rspb.1987.0035)
50. Phillips OM. 1977 *The dynamics of the upper ocean*, 2nd edn. Cambridge, UK: Cambridge University Press.
51. Nwogu OG. 2009 Interaction of finite-amplitude waves with vertically sheared current fields. *J. Fluid Mech.* **627**, 179–213. (doi:10.1017/s0022112009005850)
52. McKee WD. 1986 Reflection of water waves from an exponentially sheared current. *J. Appl. Math.* **37**, 77–90. (doi:10.1093/imamat/37.1.77)

53. Shrira VI, Ivonin DV, Broche P, de Maistre JC. 2001 On remote sensing of vertical shear of ocean surface currents by means of a single-frequency VHF radar. *Geophys. Res. Lett.* **28**, 3955–3958. (doi:10.1029/2001gl013387)
54. Bender CM, Orszag S, Orszag SA. 1999 *Advanced mathematical methods for scientists and engineers I: asymptotic methods and perturbation theory*, vol. 1. New York, NY: Springer Science & Business Media.
55. Stokes GG. 1847 On the theory of oscillatory waves. *Trans. Camb. Phil. Soc.* **8**, 441–455.
56. Whitham GB. 2011 *Linear and nonlinear waves*. New York, NY: John Wiley & Sons.
57. Lovecchio S, Climent E, Stocker R, Durham WM. 2019 Chain formation can enhance the vertical migration of phytoplankton through turbulence. *Sci. Adv.* **5**, eaaw7879. (doi:10.1126/sciadv.aaw7879)
58. Miche M. 1944 Mouvements ondulatoires de la mer en profondeur constante ou décroissante. *Annales de Ponts et Chaussées*, 26–78, 270–292, 369–406.
59. Mei CC. 1989 *The applied dynamics of ocean surface waves*, vol. 1. Singapore: World Scientific.
60. O'Malley S, Bees M. 2011 The orientation of swimming biflagellates in shear flows. *Bull. Math. Biol.* **74**, 232–55. (doi:10.1007/s11538-011-9673-1)
61. Thorpe SA. 2007 *An introduction to ocean turbulence*. Cambridge, UK: Cambridge University Press.
62. Gustavsson K, Sheikh M, Lopez D, Naso A, Pumir A, Mehlig B. 2019 Effect of fluid inertia on the orientation of a small prolate spheroid settling in turbulence. *New J. Phys.* **21**, 083008. (doi:10.1088/1367-2630/ab3062)